

# Probing $|V_{td}|$ in single-top production at $pe^\mp$ colliders

Edier Paredes Cruz, Antonio O. Bouzas and F. Larios

Departamento de Física Aplicada, CINVESTAV-IPN

Carretera Antigua a Progreso Km. 6, Apdo. Postal 73 “Cordemex”

Mérida 97310, Yucatán, México

## Abstract

We study the consequences for top-quark physics of having electron and positron beams available at the LHeC and FCC-he, as was the case in HERA. We show that the asymmetry between top production in  $pe^+$  collisions and antitop production in  $pe^-$  reactions is sensitive to  $|V_{td}|$ . By means of detailed parton-level Monte Carlo simulations of single  $t$  and  $\bar{t}$  production and its backgrounds, we parametrize the asymmetry dependence on  $|V_{td}|$  and estimate its uncertainties. Our analysis includes realistic phase-space cuts, and machine-learning binary classifiers for background rejection. We thus obtain limits on  $|V_{td}|$  that are substantially stronger than current ones, and also smaller than current projections for the HL-LHC. We have  $|V_{td}| < 1.6 \times |V_{td}^{\text{PDG}}|$  at the LHeC, at 68% C.L. with  $L_{\text{int}} = 2/\text{ab}$ .

## 1 Introduction

The Cabibbo-Kobayashi-Maskawa (CKM) matrix elements are free parameters in the Standard Model (SM), controlling the mixing among down-type quarks in the charged-current electroweak interactions. They are currently determined from low-energy physics processes. For the third row of the CKM matrix, containing the elements that involve the top quark, those are indirect determinations from experimental measurements of  $B^0-\bar{B}^0$  oscillations and kaon and  $B$ -meson decays. A global fit to those data [1], assuming the validity of the SM with three quark generations and unitarity of the CKM matrix, results, in particular, in the absolute values of the third row,

$$|V_{td}^{\text{PDG}}| = (8.57_{-0.18}^{+0.20}) \times 10^{-3}, \quad |V_{ts}^{\text{PDG}}| = (4.11_{-0.072}^{+0.083}) \times 10^{-2}, \quad |V_{tb}^{\text{PDG}}| = 0.999118_{-3.6 \times 10^{-5}}^{+3.1 \times 10^{-5}}. \quad (1)$$

In what follows we will take these values as reference. The CMS Collaboration has made a recent determination of third-row CKM matrix elements, from measurements of single-top  $t$ -channel production and decay in leptonic mode at the LHC at  $\sqrt{s} = 13$  TeV, yielding  $|V_{tb}| = 0.988 \pm 0.024$  and  $|V_{td}|^2 + |V_{ts}|^2 = 0.06 \pm 0.06$  [2]. Notice that (1) is consistent with these CMS values.

In recent years there has been an increasing interest in direct and model independent measurements of the CKM mixing parameters at hadron colliders. Measurements of the inclusive [3], or differential [4], cross sections for  $t$ -channel single-top and  $tW$  production were proposed to set direct limits on  $|V_{tq}|$ . Since a direct measurement of the flavor off-diagonal top decay modes might be a way to measure  $|V_{td}|$  and  $|V_{ts}|$ , some strategies based on light-quark tagging in  $t \rightarrow Wq$  decay have also been proposed [5, 6]. In [7] the charge asymmetry in  $tW$  associate production at the LHC due to  $d$ , unlike  $\bar{d}$ , being a valence quark in the proton, is proposed as a means to determine  $|V_{td}|$ . The sensitivity to  $|V_{td}|$  reported in [7], however, is rather low, due to a combination of sizeable backgrounds, especially  $t\bar{t}$ , and a weak dependence on  $|V_{td}|$  of the asymmetry. On the other hand, a recent global analysis of  $t$ -channel single-top and  $tW$  associate production, based on published data on inclusive and differential cross sections from the Tevatron CDF and D0, and the LHC ATLAS and CMS experiments was carried out in [8]. The global fit of [8] yields the absolute values of third-row CKM matrix elements:

$$\begin{aligned} |V_{td}| &= 0.0_{-0.000}^{+0.038}, & |V_{ts}| &= 0.0_{-0.000}^{+0.069}, & |V_{tb}| &= 0.980_{-0.012}^{+0.009}, & (\text{marginal}), \\ |V_{td}| &= 0.0_{-0.000}^{+0.023}, & |V_{ts}| &= 0.0_{-0.000}^{+0.041}, & |V_{tb}| &= 0.986_{-0.008}^{+0.008}, & (\text{individual}), \end{aligned} \quad (2)$$

where “marginal” refers to  $|V_{tk}|$ ,  $k = d, s, b$  varied independently, and “individual” to  $|V_{td}|$  or  $|V_{ts}|$  varied one at a time, with  $|V_{ts}|$  or  $|V_{td}| = 0$  and  $|V_{tb}| = 1$ . In what follows we always set the CKM third row to their values (1) and use the marginal value (2) as a baseline for our results.

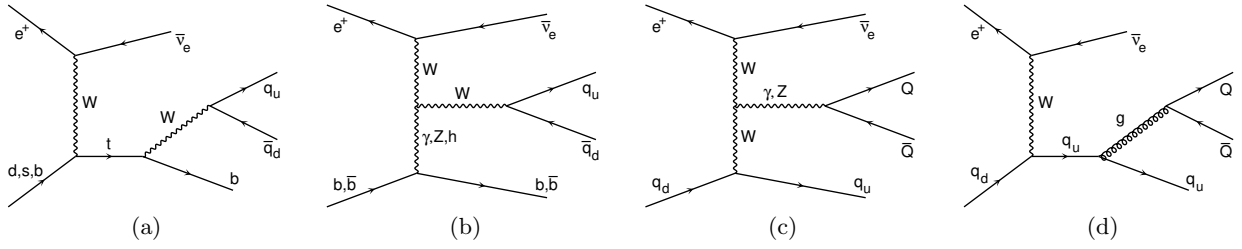


Figure 1: (a) Feynman diagrams for single-top production in  $pe^+$  collisions, in hadronic mode with flavor-diagonal decay. (b) Representative single- $W$  production diagram for the irreducible background  $B_{1b}^+$ . (c) and (d) Representative diagrams for the reducible background  $B_{0b}^+$  (with  $Q = q_u, q_d$  in (c) and  $q_u, q_d, g$  in (d)), or  $B_{2b}^+$  (with  $Q = b$ ). In all cases,  $q_u, q_d$  are as in (3). The diagrams were drawn with `MadGraph5_aMC@NLO` [24].

Electroweak top-quark production can also be probed in proton-lepton collisions. The only such collider ever operated was HERA [9, 10], which provided collisions of a proton beam with polarized electron and positron beams. HERA’s center-of-mass energy of 320 GeV and total integrated luminosity of 800/pb were sufficient to produce high-precision data on QCD and electroweak physics but not enough to observe top production. The latter will be measured at future proton-lepton colliders, such as the Large Hadron-electron Collider (LHeC) [11] (with beam energies  $E_e = 60$  GeV,  $E_p = 7$  TeV,  $\sqrt{s} = 1.3$  TeV), and the Future Circular Collider (FCC-he) [12] (with  $E_e = 60$  GeV,  $E_p = 50$  TeV,  $\sqrt{s} = 3.5$  TeV). For these  $pe$  colliders the study of the top-quark couplings to the Higgs and electroweak bosons will be among the most important areas of research [11, 12, 13, 14, 15, 16]. The dominant top-quark production mode at the LHeC and FCC-he is single-top production, followed by top pair and associate  $tW$  production [13].

HERA delivered integrated luminosities in positron runs that were comparable to those for electrons and, in its first stage, they were actually somewhat larger, see figure 4 and table 1 in [17]. A different situation is considered in the baseline design for the LHeC since, with current technology, the intensity of high-energy positron beams would be smaller than that of electron ones by a factor of 1/10–1/100 [18, 11]. There is, however, great interest at present in the development of intense positron beams for future  $e^+e^-$  colliders such as CLIC [19], the proposed muon collider [20], and the LHeC and FCC-he themselves. For the LHeC, new positron sources have been proposed [11]: one [21] would be based on photon beams from the future LHC Gamma Factory [22], and another [23] based on an LHeC-generated free-electron laser beam. Those sources would provide positron beams as intense as the electron ones. For the FCC-he, which is decades in the future, it is reasonable to assume that intense positron beams will be available when it is operating.

In this paper we study the consequences for top-quark physics of having both electron and positron beams available at the LHeC and FCC-he with similar luminosities, as was the case in HERA. For simplicity, in what follows we assume the same luminosity for  $e^\pm$  beams. We show that the asymmetry between top production in  $pe^+$  collisions and antitop production in  $pe^-$  reactions, due to the different distribution of  $d$  and  $\bar{d}$  in the proton, is sensitive to  $|V_{td}|$ . By means of detailed parton-level Monte Carlo simulations, we parametrize the asymmetry dependence on  $|V_{td}|$  and compute its statistical uncertainty. Furthermore, we carry out an in-depth study of background processes and their charge asymmetries, which contribute to the systematic uncertainty of the total asymmetry. We thus obtain limits on  $|V_{td}|$  that are substantially stronger than current ones and smaller than current projections for the HL-LHC [8].

This paper is organized as follows. In section 2 we study single-top production and decay in hadronic mode in  $pe^\pm$  collisions. We discuss the signal and background processes and their contributions to the charge asymmetry, and estimate the uncertainties in the latter, to obtain limits on  $|V_{td}|$ . In section 3, we carry out a similar analysis for the leptonic mode of single-top production. In section 4 we give our summary and final remarks. Three appendices gather results used in the previous sections. In appendix A we discuss the impact of beam polarization on the asymmetry and its sensitivity to  $|V_{td}|$ . In appendix B we derive the expression of the asymmetry for the total process in terms of those for the signal and backgrounds. In appendix C we give an accurate estimate of the statistical uncertainty of the asymmetry in terms of those of cross sections.

## 2 Asymmetry in hadronic mode

We consider in this section single-top production in  $pe^\pm$  collisions, and its decay in hadronic mode,

$$S^+ : pe^+ \rightarrow t\bar{\nu}_e \rightarrow b q_u \bar{q}_d \bar{\nu}_e, \quad S^- : pe^- \rightarrow \bar{t}\nu_e \rightarrow \bar{b} \bar{q}_u q_d \nu_e, \quad q_u = u, c, \quad q_d = d, s. \quad (3)$$

The processes  $S^\pm$  are our signal processes. We decompose them into subprocesses  $S_d^\pm$  and  $S_{sb}^\pm = S_s^\pm + S_b^\pm$ , according to the initial quark flavor. The Feynman diagrams for  $S^+$  in the SM are displayed in figure 1 (a). There are a total of 12 diagrams for  $S^+$ , all of them  $\mathcal{O}(\alpha^2)$ , which include all possible quark-flavor combinations with Cabibbo mixing only, and as many for  $S^-$ . The scattering amplitudes for  $S_d^\pm$  are proportional to  $V_{td}$ , and those for  $S_s^\pm, S_b^\pm$  to  $V_{ts}$  and  $V_{tb} \sim 1$ , respectively. Therefore, the cross section for  $S^\pm$  is dominated by that for  $S_{sb}^\pm$ ,  $\sigma_{S^\pm} = \sigma_{S_{sb}^\pm} + \sigma_{S_d^\pm} \simeq \sigma_{S_{sb}^\pm}$ . Because  $d$  is a valence quark in the proton, however, the cross section for  $S_d^+$  is substantially larger than that for  $S_d^-, S_s^\pm$ , although still much smaller than that for  $S_b^\pm$  due to CKM suppression.

The parton level processes  $S_{q_d}^+$  and  $S_{q_d}^-$  ( $q_d = d, s, b$ ) are charge conjugate of each other.<sup>1</sup> We define the charge asymmetry for a charge-conjugate pair of processes  $P^\pm$  in  $pe^\pm$  collisions, such as  $S_{q_d}^\pm$ , as

$$A_P = \frac{\sigma_{P^+} - \sigma_{P^-}}{\sigma_{P^+} + \sigma_{P^-}}, \quad (4)$$

where  $\sigma_{P^\pm}$  is the cross section for process  $P^\pm$ , which can be the signal process represented by the diagram (a) in figure 1, or one of the backgrounds described by diagrams (b)–(d) in the figure. With the parton-level cross sections computed with mild phase-space cuts

$$p_T > 4.5 \text{ GeV}, \quad |y| < 5.3, \quad (5)$$

for all quarks and gluons in the final state, the asymmetries for the signal processes and its subprocesses are  $A_{S_d} \sim \mathcal{O}(10^{-1})$ , and  $A_{S_{sb}}, A_S \sim \mathcal{O}(10^{-4})$ . Because the cross sections  $\sigma_{S^\pm}$  receive a large contribution from  $\sigma_{S_b^\pm} \gg \sigma_{S_d^\pm}$ , their dependence on  $|V_{td,ts}|$  is very weak. On the other hand, the contributions of  $S_{sb}^\pm$  to the numerator of the asymmetry  $A_S$  largely cancel, leading to a strong dependence of  $A_S$  on  $|V_{td}|$ , a more moderate one on  $|V_{tb}|$  through the denominator in (4), and a negligible dependence on  $|V_{ts}|$ . Since the current *direct* limits on  $|V_{tb}|$  bound it to within  $\pm 1\%$ , as shown in (2), the variation of  $A_S$  on that narrow range of numerical values for  $|V_{tb}|$  is not significant. Therefore, in what follows we will fix the value of  $|V_{tb}|$  to that given in (1). Our goal in this paper is to determine what level of sensitivity to  $|V_{td}|$  can be reached through an experimental measurement of  $A_S$ .

The irreducible backgrounds  $B_{1b}^\pm$  to (3) are given by the same initial and final states as  $S^\pm$ , but with  $bq\bar{q}$  not originating in a top decay. They involve 774 diagrams each, out of which 674 are purely electroweak  $\mathcal{O}(\alpha^2)$ , such as the single- $W$  production diagram shown in Figure 1 (b), and the remaining 100 contain two QCD vertices and are  $\mathcal{O}(\alpha\alpha_s)$ . The cross sections for  $B_{1b}^\pm$ , computed with the lax phase-space cuts (5), is a few percent of that for  $S_b$ . It is dominated by diagrams with a  $b$  (anti)quark in the initial state since diagrams with a lighter initial parton are suppressed by one power of  $V_{ub,cb}$  (or  $V_{td,ts}$  in diagrams with a  $t$ -channel top). Because of this, as we discuss more quantitatively below, the contribution to the asymmetry from this process is small compared to that of the signal process. This background is, therefore, easily controlled.

There are two types of reducible backgrounds. The first one consists of processes of the form

$$pe^+ \rightarrow j_1 j_2 j_3 \bar{\nu}_e, \quad pe^- \rightarrow j_1 j_2 j_3 \nu_e, \quad (6)$$

with  $j_n$  light partons. This includes top-production processes with a  $b$ -quark in the initial state and the top decaying to  $jW$ . For those processes, the cross section is suppressed by one power of  $V_{td,ts}$  relative to  $S_b$ , as with  $S_d$ , and their asymmetry is as small as that of  $S_{sb}$ . Thus, as shown in Appendix B, their contribution to the total asymmetry is negligibly small. We will not consider those processes further here.<sup>2</sup> We denote  $B_{0b}^\pm$  the reducible background processes (6) not involving top production. Those are given by 1440 Feynman diagrams each, out of which 1184 have electroweak vertices only ( $\mathcal{O}(\alpha^2)$ ) and 256 have two QCD vertices ( $\mathcal{O}(\alpha\alpha_s)$ ). Two representative diagrams for  $B_{0b}^+$  are shown in Figure 1 (c) with  $Q = q_u, q_d$ , and (d) with

<sup>1</sup>More specifically, the initial states of  $S_{q_d}^\pm$  are charge conjugate of each other in the unpolarized case. In what follows, we will always assume unpolarized beams except in appendix A

<sup>2</sup>However, we have taken these backgrounds fully into account in the computations of cross sections and asymmetries described below, thus explicitly verifying their smallness.

$Q = q_u, q_d, g$ . The cross section for  $B_{0b}^\pm$ , computed with the loose parton-level cuts (5), is about six times larger than that of  $S$ . Furthermore, due to the subprocesses of (6) with initial valence quarks,  $B_{0b}$  has a large asymmetry  $A_{B_{0b}}$ . These features make  $B_{0b}^\pm$  the most important, difficult to control backgrounds.

The second type of reducible background is given by processes of the form (6) with  $j_{1,2} = b$  or  $\bar{b}$ , and  $j_3$  a lighter parton. This includes top-production processes with a  $b$ -quark in the initial state and the decay chain  $t \rightarrow bW \rightarrow b\bar{b}q_u$  or its charge conjugate. Similarly to the previous case  $B_{0b}$ , those processes have both small cross section and small asymmetry, so we will not consider them further.<sup>2</sup> We denote  $B_{2b}^\pm$  the reducible background processes (6) with two  $b$  quarks in the final state not involving top production. Those are given by 188 Feynman diagrams each, out of which 172 have electroweak vertices only, and 16 have two QCD vertices. Their nominal perturbative orders are as for  $B_{0b}$ . Two representative diagrams for  $B_{2b}^\pm$  are shown in Figure 1 (c), (d) with  $Q = b$ . The cross section for  $B_{2b}^\pm$ , computed with the parton-level phase-space cuts described above, is about 20 times smaller than that of  $S$  at the LHeC energy, and about 50 times smaller at the FCC-he. However,  $B_{2b}$  has a large asymmetry  $A_{B_{2b}}$ , due to the valence quarks in the initial state of  $B_{2b}^\pm$ , which makes it the second most important background to the signal  $S$  (3).

The other top production processes in a  $pe$  collider are top-pair production,  $ge \rightarrow t\bar{t}e$ , and associate  $tW$  production,  $be \rightarrow tWe$ . Both are neutral current (NC) processes, with a cross section an order of magnitude smaller [13] than the single-top production (3), and a vanishing asymmetry (4) at tree level. Furthermore, due to their very different final states compared to (3), they should not contribute to the signal cross section or asymmetry. Another NC process worth mentioning is single  $W$  production in association with a  $b$  quark, which contains the subprocess  $ue^+ \rightarrow W^+be^+ \rightarrow q_u\bar{q}_d be^+$  having an asymmetry  $A$ , as in (4), proportional to  $|V_{ub}|$ . Other NC processes with  $b$ -quark or gluon in the initial state, such as  $be^+ \rightarrow bgge^+$  or  $ge^+ \rightarrow gb\bar{b}e^+$ , are symmetric at tree level. All this NC processes are rejected with perfect efficiency by the cuts (7) at the parton level, due to the absence of missing transverse energy, and with the inclusion of a veto on additional charged leptons in the final state.

We compute the tree-level cross section for single-top production and its backgrounds with the matrix-element Monte Carlo generator **MadGraph5\_aMC@NLO** (henceforth MG5) version 2.6.3 [24]. We use the parton distribution function (PDF) **CTEQ66** from the library **LHAPDF6** [25]. We carry out the event analysis with **ROOT** version 6.22 [26], including the Toolkit for Multivariate Analysis, **TMVA** [27]. We apply in our MG5 simulations the mild, flavor-blind cuts (5) to avoid infrared divergences in background processes. We perform event pre-selection in our ROOT analysis. We  $b$ -tag partons in each event by assigning to each parton a tag  $\tau_b(J) = 0$  if  $J$  is a light parton, and 1 if it is a  $b$  quark. Here,  $J_{0,1,2}$  are the final state partons (“jets”) ordered by decreasing  $p_T$ . We use a working point with a  $b$ -tagging efficiency  $\eta_b = 0.85$ , and mistagging probabilities  $p_c = 0.1$  for  $c$  quarks and  $p_j = 0.01$  for lighter partons. We then apply the following phase-space cuts on  $b$ -tagged events,

$$\begin{aligned} |y(J)| &< 5.0, \quad |y(J_b)| < 3.0, \\ p_T(J) &> 5.0 \text{ GeV}, \quad \Delta R(J, J') > 0.4, \quad \cancel{E}_T > 10.0 \text{ GeV}, \\ 142.0 &< m(J_0, J_1, J_2) < 202.0 \text{ GeV}. \end{aligned} \tag{7}$$

On the first line of this equation we require all partons ( $J$ ) to be inside the detector, and  $b$ -tagged ones ( $J_b$ ) in the central region where  $b$ -tagging is operational and efficient. On the second line of (7) we impose minimal  $p_T$  and isolation requirements on all final-state particles. On the third line we require that the three final-state partons reconstruct the top mass.

The asymmetry  $A$  in (4) depends non-linearly on the signal and background cross sections. As discussed in detail in appendix B, because of this non-linearity, the measured asymmetry  $A$  is given in terms of the signal and backgrounds asymmetries  $A_S, A_{B_0}, \dots$ , as a sum of weighted asymmetries  $\tilde{A}_S, \tilde{A}_{B_0}, \dots$ , with weights that are ratios of cross sections. The exact expression for these asymmetries  $\tilde{A}$  is given in equation (23). In Table 1 we show the cross sections and the associated asymmetries  $A$  from (4) and  $\tilde{A}$  from (23), for the signal (3), the irreducible background  $B_{1b}$  and the reducible backgrounds  $B_{0b}, B_{2b}$ , at LHeC and FCC-he energies, with the cuts (7). The large asymmetries of the reducible background processes can be seen in that table.

The signal processes  $S$ , (3), and the background processes  $B_{kb}$ ,  $k = 0, 1, 2$ , have different phase-space distributions, which we can use to reject backgrounds. We resort to standard machine-learning methods such as boosted-decision trees (BDTs) (see, e.g., [28] and refs. therein) that are known to be effective tools to optimize background rejection. For instance, BDTs were applied in LHC analyses of Higgs production and decay [29, 30]. We use gradient-boosted BDTs (BDTGs), implemented in the TMVA [27] framework with  $10^3$  trees and default parameters. In all cases we use a set of  $10^6$  events passing the cuts (7) for training,

		LHeC				FCC-he			
cuts		$S$	$B_{1b}$	$B_{0b}$	$B_{2b}$	$S$	$B_{1b}$	$B_{0b}$	$B_{2b}$
(7)	$\sigma_{P+}$ [fb]	952.261	17.933	4117.950	30.243	7826.525	116.790	22609.2	103.833
	$\sigma_{P-}$ [fb]	950.786	17.934	5458.860	50.152	7829.969	116.402	23752.2	116.472
	$A \times 10^4$	7.752	-0.223	-1400	-2476	-2.200	16.64	-246.5	-573.7
	$\tilde{A} \times 10^4$	1.272	-0.0006899	-1156	-17.27	-0.5513	0.06211	-183	-2.023
(7)+(9)	$\sigma_{P+}$ [fb]	115.625	0.110	0.827	0.0142	1253.402	1.0409	4.438	0.0434
	$\sigma_{P-}$ [fb]	114.831	0.111	0.795	0.0285	1253.620	1.067	4.715	0.0468
	$A \times 10^4$	34.44	-37.44	191.7	-3351	-0.8698	-125.6	-302.8	-372.8
	$\tilde{A} \times 10^4$	34.16	-0.03564	1.343	-0.6166	-0.8658	-0.1051	-1.101	-0.01335

Table 1: Cross sections in fb and their associated asymmetries  $A$ , (4), and  $\tilde{A}$ , (23), at LHeC and FCC-he energies. The results of applying both the cuts (7) and those plus (9) are shown. Asymmetries are computed from cross sections before rounding the latter to three decimal digits at most.

and a separate, independent set of  $5 \times 10^5$  to  $10^6$  events for application. Furthermore, we apply the trained BDTGs also on the combined training-plus-application data for control.

We use three different classifiers: first, we train a BDTG with the process  $S_d^+$  as signal and  $B_{0b}^+$  as background, denoted  $\text{BDT}(S_d^+/B_{0b}^+)$ , to suppress  $B_{0b}^+$  with respect to the signal. Second, similarly, we train a  $\text{BDT}(S_d^+/B_{2b}^+)$  to reject the backgrounds  $B_{2b}^+$ . Third, we also train a BDT with  $S_d^+$  as signal and  $S_d^-$  as background,  $\text{BDT}(S_d^+/S_d^-)$ , to enhance the signal asymmetry. Each BDT is trained with 28 kinematic variables, containing the rapidities  $y$ , transverse momenta  $p_T$ , azimuthal angles  $\varphi$ , and invariant masses of one or more partons. We consider also the  $p_T$  and  $\varphi$  of the missing transverse energy, corresponding to the neutrino in (3). We also include the  $b$ -tags  $\tau_b$  defined above, the number  $N_b$  of  $b$  quarks, the phase-space distances among partons  $\Delta R = \sqrt{(\Delta y)^2 + (\Delta \varphi)^2}$ , and the cosine  $\cos(\theta_{Wj}^*)$  of the angle between the 3-momenta of the reconstructed  $W$  and its decay product with the largest  $p_T$  in the rest frame of the reconstructed  $W$  (analogous to the leptonic variable defined in [31], see next section). Furthermore, we consider the cosine  $\cos(\theta_{\text{jspect}})$  of the angle between the  $W$  decay-product with largest  $p_T$  and the parton not coming from  $W$  decay, or “spectator,” in the lab frame, the cosine  $\cos(\theta_{J_0 J_1})$  of the angle between the three-momenta of  $J_{0,1}$  in lab frame, the sphericity  $S_{\text{chrgd}}$  and aplanarity  $A_{\text{chrgd}}$  for charged particles, as defined in chapter 9 of [32], and also the “visible”  $S_{\text{vsbl}}$ ,  $A_{\text{vsbl}}$ , computed with the four-momenta of the charged particles and the missing four-momentum  $p^\mu = (|\vec{p}_T|, \vec{p}_T^x, \vec{p}_T^y, 0)$ . The 20 variables highest ranked in BDTG training for each signal and background combination are as follows:

$$\begin{aligned}
S_d^+/S_d^- : & y(J_0, J_1, J_2), \varphi(J_1), p_T(\not{E}_T), \varphi(J_2), \varphi(J_0, J_1, J_2), y(J_2), \Delta R_{(J_0, J_2)}, \varphi(\not{E}_T), m_{(J_1, J_2)}, \cos(\theta_{Wj}^*), \varphi(J_0), \\
& S_{\text{chrg}}, \Delta R_{(J_0, J_1)}, p_T(J_2), \Delta R_{(J_1, J_2)}, m_{(J_0, J_1)}, y(J_1), \cos(\theta_{J_0 J_1}), p_T(J_1), m_{(J_0, J_2)}, \\
S_d^+/B_{0b}^+ : & m_{(J_0, J_1, J_2)}, m_{(J_1, J_2)}, m_{(J_0, J_2)}, m_{(J_0, J_1)}, p_T(\not{E}_T), y(J_0, J_1, J_2), p_T(J_2), y(J_0), y(J_2), p_T(J_0), \cos(\theta_{Wj}^*), \\
& \tau_b(J_1), p_T(J_1), \cos(\theta_{Wj}^*), \tau_b(J_2), y(J_1), \tau_b(J_0), N_b, \Delta R_{(J_1, J_2)}, S_{\text{vsbl}}, \\
S_d^+/B_{2b}^+ : & m_{(J_0, J_1)}, m_{(J_0, J_2)}, m_{(J_1, J_2)}, m_{(J_0, J_1, J_2)}, \tau_b(J_0), \tau_b(J_1), p_T(\not{E}_T), y(J_2), \cos(\theta_{Wj}^*), y(J_0, J_1, J_2), N_b, \\
& y(J_0), \tau_b(J_2), y(J_1), A_{\text{chrgd}}, p_T(J_0), p_T(J_2), \cos(\theta_{\text{jspect}}), p_T(J_1), \Delta R_{(J_0, J_2)}.
\end{aligned} \tag{8}$$

In the first line we see that the most discriminating variable is the top rapidity, which is clearly related to the process  $S_d^+$  being initiated by a valence quark, unlike  $S_d^-$ . Similarly, on the second and third lines of (8), the highest ranked variables are masses and  $b$ -tags, as expected for reducible backgrounds less resonant than the signal. In figure 2 we display the differential cross section at the LHeC energy with respect to the score variable for the signal and background processes for the three BDTs trained as in (8). The corresponding results for the FCC-he are similar to those for the LHeC in figure 2. Those distributions motivate us to apply the following selection cuts on our event samples to reject the backgrounds,

$$x_{S_d^+ S_d^-} > 0.0, \quad x_{S_d^+ B_{0b}^+} > 0.99, \quad x_{S_d^+ B_{2b}^+} > 0.96, \tag{9}$$

where  $x_{P_1 P_2}$  refers to the score variable generated by  $\text{BDT}(P_1/P_2)$  trained with process  $P_1$  as signal and  $P_2$  as background, as described above. The cross sections and asymmetries for the signal and background processes computed with the preselection cuts (7) and the selection ones (9) are shown in Table 1. We notice,

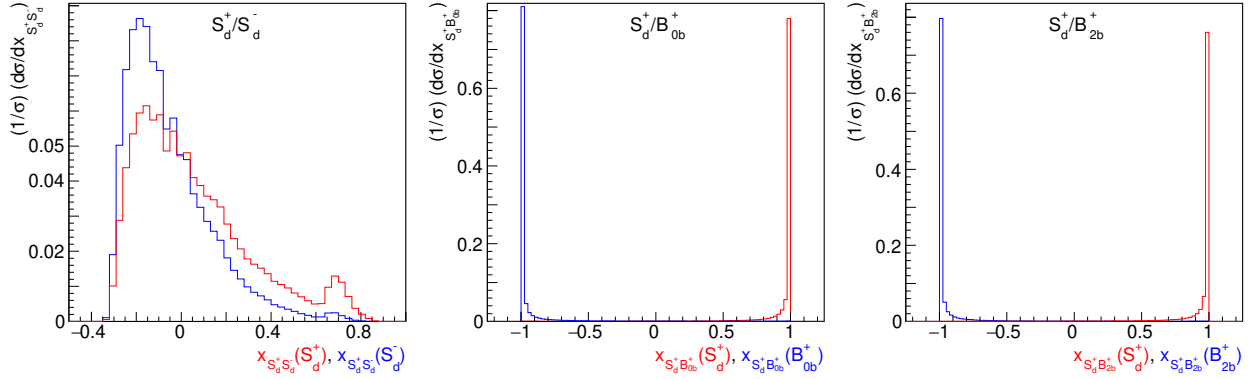


Figure 2: Normalized differential cross sections with respect to the score variable for the signal (red line) and background (blue line), at the LHeC energy, for three BDTs trained with the signal-and-background pairs indicated.

from the table, the high degree of background rejection, which, in turn, leads to the signal asymmetries  $A_S$  and  $\tilde{A}_S$  being approximately equal, and the background ones  $\tilde{A}_B$  ( $B = B_{kb}$ ,  $k = 0, 1, 2$ ) being smaller than that of the signal, especially at the LHeC.

We stress here that the cuts on score variables (9) play a role completely analogous to phase-space cuts in cut-based analyses such as [7]. In fact, the cuts (9) entail cuts on the phase-space variables (8) used to compute the score variables. Thus, using a BDT provides optimized phase-space cuts on the relevant kinematic variables. In particular, the cut on  $x_{S_d^+ S_d^-}$  selects the phase-space region where the asymmetry is largest. Notice that in [7], section III B is dedicated to finding an optimal set of cuts to maximize the charge asymmetry defined in that reference. By using the cut on  $x_{S_d^+ S_d^-}$  in (9), we enable the BDT to find the optimal region for us.

In order to estimate the total uncertainty in the asymmetry  $A$ , we take into account the background contributions to it,  $\tilde{A}_B$ , the statistical uncertainties as described in appendix C, eq. (26), and the systematic uncertainties related to the choice of PDF and its scale. The latter are provided by MG5 and the library LHAPDF6 for the cross sections, and propagated to the asymmetry as in appendix C. We obtain uncertainties of 4.5% (scale) and 3.34% (PDF) at the LHeC, and 23.5% (scale) and 35.7% (PDF) at the FCC-he. The relative asymmetry uncertainties at the FCC-he are significantly larger than those at the LHeC due to the smallness of the asymmetry in the former collider relative to the latter. Obtaining an estimate of systematic uncertainties related to finite energy resolution and other detector effects is beyond the scope of this paper. However, since the uncertainty in the asymmetry is dominated by the statistical one, we expect those other systematic uncertainties to have a moderate impact on the total uncertainty. We obtain our estimate of the total asymmetry uncertainty  $\Delta_{\tilde{A}_S, \text{tot}}$  by adding in quadrature the three types of uncertainty mentioned above: statistical, background and systematic.

To obtain bounds on  $|V_{td}|$ , we consider the dependence on it of the signal asymmetry  $\tilde{A}_S(|V_{td}|)$ . For a given total uncertainty, the allowed values for  $|V_{td}|$  are determined with statistical significance  $\mathcal{S}$  ( $\mathcal{S} = 1, 2, \dots$ ) by the inequality

$$\tilde{A}_S(|V_{td}|) < \tilde{A}_S^{\text{SM}} + \mathcal{S} \Delta_{\tilde{A}_S, \text{tot}}, \quad (10)$$

where  $\tilde{A}_S^{\text{SM}} = \tilde{A}_S(|V_{td}^{\text{PDG}}|)$  and  $|V_{td}^{\text{PDG}}|$  from (1). We parametrize  $\tilde{A}_S(|V_{td}|)$  as,

$$\tilde{A}_S(|V_{td}|) = \tilde{A}_S^{\text{SM}} + a \left( \frac{|V_{td}|}{|V_{td}^{\text{PDG}}|} - 1 \right) + b \left( \frac{|V_{td}|}{|V_{td}^{\text{PDG}}|} - 1 \right)^2, \quad (11)$$

with  $|V_{td}^{\text{PDG}}|$  from (1). We determine the parameters in (11) from an extensive set of Monte Carlo simulations at each energy, to which (11) is fitted. We obtain excellent fits with  $a = 2.117 \times 10^{-3}$ ,  $b = 9.511 \times 10^{-4}$  at the LHeC, and  $a = 1.185 \times 10^{-4}$ ,  $b = 5.858 \times 10^{-5}$  at the FCC-he. These parameter values, as well as their 68% and 95% CL intervals shown in figure 3, were computed with Mathematica [33]. Notice that these values imply, in particular, that the asymmetry  $\tilde{A}_S(|V_{td}|)$  is an increasing function of  $|V_{td}|$ . This is very different from the asymmetry defined in [7] in the context of  $pp$  collisions at the LHC, which is a *decreasing* function of  $|V_{td}|$ , as shown in figure 5 of [7].

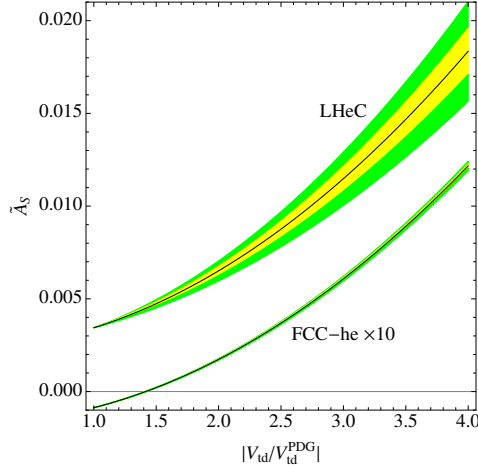


Figure 3: The polynomial fits (11) with the parameters given in the text, at the LHeC and FCC-he energies, with 68% (yellow) and 95% (green) CL bands.

C.L.	LHeC				FCC-he			
	68%		95%		68%		95%	
$L_{\text{int}} [1/\text{ab}]$	1	2	1	2	1	2	1	2
$ V_{td} / V_{td}^{\text{PDG}}  <$	1.80	1.61	2.34	2.04	2.99	2.59	4.10	3.52

Table 2: Limits on  $|V_{td}|$  obtained from simulated charge-asymmetry measurements in single-top production in hadronic mode in  $pe^\pm$  collisions. Results are shown for two values of Confidence Level corresponding to  $S = 1, 2$ , and two values of integrated luminosity. The value of  $|V_{td}^{\text{PDG}}|$  is given in (1).

Substituting (11) into (10) yields an upper bound on  $|V_{td}|$ . These bounds are the main results of this paper. They are reported in Table 2, at statistical significance  $S = 1, 2$ , for two values of integrated luminosity at the energies of the LHeC and FCC-he. We see from the table that the limits obtained at the LHeC energy are stricter than those at the FCC-he, as expected, since due to the evolution of the proton PDF with the energy scale, the asymmetry is expected to be smaller at higher energies, and its dependence on  $|V_{td}|$  correspondingly weaker.

The best current direct bounds on  $|V_{tk}|$ ,  $k = d, s, b$ , are obtained in [8] from LHC data, as shown above in (2). With the notation of table 2 and (1), those values and the projection for the HL-LHC [8], are written as,

$$\frac{|V_{td}|}{|V_{td}^{\text{PDG}}|} < \begin{cases} 4.43 & \text{(LHC marginal)} \\ 2.68 & \text{(LHC individual)} \\ 2.89 & \text{(HL-LHC)} \end{cases} \quad (68\% \text{C.L.}). \quad (12)$$

We stress the large difference between the marginal and individual LHC limits in this equation, arising from the global analysis in [8] being based on observables having a strong dependence on  $|V_{tb}|$ , but a poor one on  $|V_{td,ts}|$ . On the other hand, as discussed in the text under (5), the asymmetry (4) is sensitive to  $|V_{td}|$ , but has little variation over the interval of  $|V_{tb}|$  determined by the direct bounds (2) from [8]. Thus, in a global analysis of third-row CKM parameters including the asymmetry  $A$ , there should be a small difference between marginal and individual limits on  $|V_{td}|$ . In this sense, the 68% CL limits on  $|V_{td}|$  reported in table 2 should be compared to the marginal limits in (12). We notice, however, that the results in table 2 at the LHeC energy, at 68% CL, are substantially stronger than even the individual limit in (12).

### 3 Leptonic mode

In leptonic mode the signal processes take the form

$$S^+ : pe^+ \rightarrow t\bar{\nu}_e \rightarrow b\ell^+\nu_\ell\bar{\nu}_e, \quad S^- : pe^- \rightarrow \bar{t}\nu_e \rightarrow \bar{b}\ell^-\bar{\nu}_\ell\nu_e, \quad \ell = e, \mu, \quad (13)$$

to be compared to (3). The asymmetry of the signal is smaller in leptonic mode than in hadronic mode: with the cuts (7),  $A_S$  is about one-third of its hadronic mode value. The leptonic-mode analogs of the irreducible backgrounds  $B_{1b}^\pm$  and the reducible one  $B_{0b}^\pm$  are obtained, similarly to the signal (13), by replacing a pair of light partons with a lepton-neutrino pair. In this mode there are no background processes analog to  $B_{2b}^\pm$ , with two  $b$  quarks in the final state. Background processes have smaller cross sections relative to signal than in hadronic mode. With the cuts (7), the irreducible background  $B_{1b}^\pm$  cross section remains at about 2% that of the signal, as in hadronic mode. On the other hand, the reducible backgrounds  $B_{0b}^\pm$  cross sections are 36% that of the signal in this mode, compared to six times larger than the signal in hadronic mode.

Because there are two neutrinos in the final state, their three-momenta cannot be easily reconstructed, so we use all kinematic variables analogous to those in (8) related to the final-state charged particles,  $b$  and  $\ell$ . However, we also approximately reconstruct the three-momentum of the neutrino produced in  $t$  decay,  $\nu_{\text{pr}}$ , by minimizing the function

$$\chi^2 = \frac{1}{\Gamma_t^2} (m(J, \ell, \nu_{\text{pr}}) - m_t)^2 + \frac{1}{\Gamma_W^2} (m(\ell, \nu_{\text{pr}}) - m_W)^2 \quad (14)$$

with respect to  $\vec{p}(\nu_{\text{pr}})$ , with the mass and decay width parameters from [1]. With this three-momentum, we can reconstruct the top and  $W$  momenta, and the transverse momentum of the scattered neutrino  $\nu_{\text{sc}}$  as missing transverse momentum.

Similarly to the hadronic mode discussed in the previous section, we train two BDTs: one,  $\text{BDT}(S_d^+/B_{0b}^+)$ , to suppress  $B_{0b}^\pm$  with respect to the signal; the other,  $\text{BDT}(S_d^+/S_d^-)$ , to enhance the signal asymmetry. We use 25 variables to train the BDTs. The 20 highest ranked for each signal and background combination are as follows:

$$\begin{aligned} S_d^+/S_d^- : & m_{(J,\ell)}, y_{(\ell)}, y_{(J,\ell)}, y_{(J)}, y_{(J,\ell,\nu_{\text{pr,rc}})}, \cos(\theta_{W\ell}^*), p_T(J), p_T(\ell), \varphi(J), m_{T(W_{\text{rc}})}, \\ & \varphi(\ell), E_{(J)}, P_{\text{vsbl}}, \Delta\varphi(\nu_{\text{pr,rc}}, \nu_{\text{sc,rc}}), dR_{(J,\ell)}, m_{T(t_{\text{rc}})}, S_{T\text{chrg}}, S_{T\text{vsbl}}, S_{\text{chrg}}, \varphi_{(J,\ell)}, \\ S_d^+/B_{0b}^+ : & p_T(\ell), p_T(J), m_{(J,\ell)}, p_T(J,\ell), y_{(J)}, y_{(\ell)}, N_b, y_{(t_{\text{rc}})}, E_{(\ell)}, \Delta R_{(J,\ell)}, \cos(\theta_{W\ell}^*), \\ & m_{T(t_{\text{rc}})}, \Delta\varphi(\nu_{\text{pr,rc}}, \nu_{\text{sc,rc}}), E_{(J)}, P_{\text{vsbl}}, S_{T\text{chrg}}, m_{T(W_{\text{rc}})}, \cos(\theta_{J\ell}), S_{T\text{vsbl}}, A_{\text{vsbl}}. \end{aligned} \quad (15)$$

The variable  $\theta_{W\ell}^*$  is the angle between the directions of the charged-lepton and the  $W$  3-momenta in the  $W$  rest frame [31]. The sphericities and aplanarities  $S_{\text{chrgd,vsbl}}$ ,  $A_{\text{chrgd,vsbl}}$ , for charged particles and “visible” ones, are defined as in the previous section above (8). In the leptonic case we also include the planarity  $P = (2/3)(S - 2A)$  and the transverse sphericity  $S_T$  [34], both charged and visible. Because the background cross sections are smaller, softer cuts than in hadronic mode (9) can be used to suppress them,

$$x_{S_d^+ S_d^-} > 0.0, \quad x_{S_d^+ B_{0b}^+} > 0.9, \quad (16)$$

We have applied the cuts on score variables for BDTs trained with the 25 variables described above, and also for BDTs trained without reconstructed variables. Comparison of the two methods shows that the inclusion of reconstructed variables improves background rejection by 20%.

The dependence of the asymmetry  $\tilde{A}_S$  on  $|V_{td}|$  is quadratic, and we parametrize it as in (11). In leptonic mode that dependence is weaker than in the hadronic one, with  $a = 1.471 \times 10^{-3}$ ,  $b = 7.016 \times 10^{-4}$  at the LHeC and  $a = 1.098 \times 10^{-4}$ ,  $b = 5.413 \times 10^{-5}$  at the FCC-he. As in the hadronic mode, the parameters for the LHeC are roughly 15 times larger than those for the FCC-he. On the other hand, the parameters  $a$ ,  $b$  in hadronic mode are approximately 40% larger than those in leptonic mode at the LHeC, and about 10% larger at the FCC-he. That weaker dependence results in a reduced sensitivity to  $|V_{td}|$  in leptonic mode, as reflected in the limits shown in table 3, which are weaker than those from hadronic mode in table 2. We notice, however, that the 68% C.L. limits in table 3 are all smaller than the marginal limit in (12).

## 4 Final remarks

In this work we considered the possibility that the LHeC and the FCC-he will run not only in  $pe^-$  but also in  $pe^+$  mode, with similar luminosities in both modes, as HERA did. In that case, the charge asymmetry in single-top production in  $pe^\mp$  collisions is sensitive to  $|V_{td}|$ .

In the hadronic mode of single-top production, BDTs provide sufficient background suppression to obtain bounds on  $|V_{td}|$ , at the parton level, that are substantially more restrictive than current experimental ones. As reported in table 2, at the LHeC energy we obtain  $|V_{td}|/|V_{td}^{\text{PDG}}| < 1.80$  at 68% C.L. with  $L_{\text{int}} = 1/\text{ab}$ , and



C.L.	LHeC				FCC-he			
	68%		95%		68%		95%	
$L_{\text{int}}$ [1/ab]	1	2	1	2	1	2	1	2
$ V_{td} / V_{td}^{\text{PDG}}  <$	2.28	2.00	3.06	2.63	4.32	3.68	6.03	5.10

Table 3: Limits on  $|V_{td}|$  obtained from simulated charge-asymmetry measurements in single-top production in leptonic mode in  $pe^\pm$  collisions. Results are shown for two values of Confidence Level corresponding to  $S = 1, 2$ , and two values of integrated luminosity.

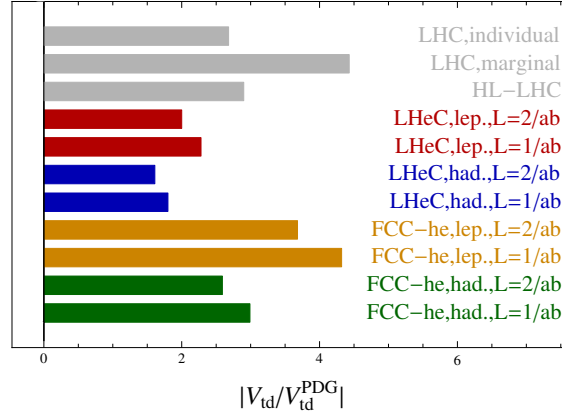


Figure 4: Limits on  $|V_{td}|$  at 68% CL from single-top production at the LHeC and FCC-he in hadronic and leptonic mode, see tables 2, 3, and from [8], see eq. (12).

$< 1.6$  with  $L_{\text{int}} = 2/\text{ab}$ , which are significantly better than the current LHC limits (12) of 4.43 (marginal). Our limits are also smaller than those projected for the HL-LHC in table 4 of [8],  $|V_{td}|/|V_{td}^{\text{PDG}}| < 2.89$  (68% CL). At the FCC-he the asymmetry in single-top production is smaller than at the LHeC, and has a weaker dependence on  $|V_{td}|$ , so that the bounds obtained are weaker than at the LHeC, though still stronger than the marginal ones in (12), as also shown in table 2. In leptonic mode the dependence of the asymmetry  $\tilde{A}_S$  on  $|V_{td}|$  is weaker than in hadronic mode. This leads to looser limits on  $|V_{td}|$ , as shown in table 3, even though the backgrounds in that mode are smaller than in the hadronic one. Still the limits obtained at 68% C.L. at the LHeC are stricter than the current ones in (12) from [8]. The 68% CL limits on  $|V_{td}|$  from tables 2 and 3, and from [8] as shown in (12), are summarized in figure 4.

We expect to carry out a more detailed analysis including QCD evolution and fast detector simulation. More importantly, by including other observables in the analysis besides the charge asymmetry studied here, the sensitivity to  $|V_{td}|$  of single-top production in  $pe^\pm$  collisions could be improved, both at the LHeC and especially at the FCC-he. In addition, we will address the possibility of potential contributions that may appear at the NLO level. We do not expect them to change the conclusions reached here because, in contrast to the LHC study made in [7], at the LHeC both signal and background contributions to the asymmetry appear already at LO. We will report those results elsewhere.

We remark, finally, that because the  $pe^\pm$  asymmetry in single-top production has a different dependence on third-generation CKM matrix elements from that of top observables in hadron colliders, due to the distinct underlying physics, its measurement would make a very important contribution to future global analyses comprising data from the LHC, HL-LHC, LHeC, future  $e^+e^-$  and/or  $\mu^+\mu^-$  colliders, and the FCC-hh and FCC-he.

**Acknowledgements** We thank Georgina Espinoza Gurriz for assistance with computer hardware. This work was partially supported by Sistema Nacional de Investigadores de Mexico.

**Data Availability Statement** No data associated in the manuscript.

## References

- [1] R. L. Workman *et al.* (Particle Data Group), Prog. Theor. Exp. Phys. **2022** (2022) 083C01.
- [2] The CMS Collaboration, “Measurement of CKM matrix elements in single top quark  $t$ -channel production in proton-proton collisions at  $\sqrt{s} = 13$  TeV,” Phys. Lett. B **808** (2020) 135609 [arXiv:2004.12181 [hep-ex]].
- [3] H. Lacker, A. Menzel, F. Spettel, D. Hirschebühl, J. Lück, F. Maltoni, W. Wagner, M. Zaro, “Model-independent extraction of  $|V_{tq}|$  matrix elements from top-quark measurements at hadron colliders,” Eur. Phys. J. C **72** (2012) 2048, [arXiv:1202.4694 [hep-ph]].
- [4] J. A. Aguilar-Saavedra, A. Onofre, “Using single top rapidity to measure  $|V_{td}|$ ,  $|V_{ts}|$ ,  $|V_{tb}|$  at hadron colliders,” Phys. Rev. D **83** (2011) 073003, [arXiv:1002.4718 [hep-ph]].
- [5] W. Jang, J. S. Hun Lee, I. Park, I. J. Watson, “Measuring  $|V_{ts}|$  directly using strange-quark tagging at the LHC,” J. Korean Phys. Soc. **81** (2022) 377. [arXiv:2112.01756 [hep-ph]].
- [6] D. A. Faroughy, J. F. Kamenik, M. Szewc, J. Zupan, “Accessing CKM suppressed top decays at the LHC,” [arXiv:2209.01222 [hep-ph]].
- [7] E. Alvarez, L. Da Rold, M. Estevez, J. F. Kamenik, “Measuring  $|V_{td}|$  at the LHC,” Phys. Rev. D **97** (2018) 033002 [arXiv:1709.07887 [hep-ph]].
- [8] B. Clerbaux, W. Fang, A. Giammanco, R. Goldouzian, “Model-independent constraints on the CKM matrix elements  $|V_{tb}|$ ,  $|V_{ts}|$  and  $|V_{td}|$ ,” JHEP **03** (2019) 022 [arXiv:1807.07319 [hep-ph]].
- [9] O. Brüning, A. Seryi, S. Verdú-Andrés, “Electron-Hadron Colliders: EIC, LHeC and FCC-eh,” Frontiers in Physics, **10** (2022) 886473.
- [10] F. Willeke, “The HERA lepton-proton collider,” chapter 15 of O. Brüning, S. Myers (Editors), “Challenges and Goals for Accelerators in the XXI Century,” World Scientific, Singapore, 2021.
- [11] P. Agostini *et al.* [LHeC and FCC-he Study Group], “The Large Hadron-Electron Collider at the HL-LHC,” J. Phys. G **48** (2021) 110501. [arXiv:2007.14491 [hep-ex]].
- [12] A. Abada, *et al.*, “FCC Physics Opportunities,” Eur. Phys. J. C **79** (2019) 474.
- [13] A. Bouzas, F. Larios, “Probing  $tt\gamma$  and  $ttZ$  couplings at the LHeC,” Phys. Rev. D **88** (2013) 094007 [arXiv:1308.5634 [hep-ph]].
- [14] I. A. Sarmiento-Alvarado, A. O. Bouzas, F. Larios, “Analysis of top-quark charged-current coupling at the LHeC,” J. Phys. G **42** (2015) 085001 [arXiv:1412.6679 [hep-ph]].
- [15] S. Dutta, A. Goyal, M. Kumar, B. Mellado, “Measuring anomalous  $Wtb$  couplings at  $e^-p$  collider,” Eur. Phys. J. C **75** (2015) 577 [arXiv:1307.1688 [hep-ph]].
- [16] G. R. Boroun, “Top cross section in the LHeC and FCC-he energy range,” Phys. Lett. B **838** (2023) 137712 [arXiv:2301.03261 [hep-ph]].
- [17] D. M. South, M. Turcato, “Review of Searches for Rare Processes and Physics Beyond the Standard Model at HERA,” Eur. Phys. J. C **76** (2016) 336 [arXiv:1605.03459 [hep-ex]].
- [18] J. L. Abelleira *et al.* [LHeC Study Group], “A Large Hadron Electron Collider at CERN, Report on the Physics and Design Concepts for Machine and Detector,” J. Phys. G **39** (2012) 075001 [arXiv:1206.2913 [physics.acc-ph]].
- [19] M. Aicheler *et al.* editors, “The Compact Linear Collider (CLIC) - Project Implementation Plan,” CERN Yellow Reports 4/2018 [arXiv:1903.08655 [physics.acc-ph]].
- [20] C. Accettura, D. Adams, R. Agarwal *et al.*, “Towards a muon collider,” Eur. Phys. J. C **83** (2023) 864 [arXiv:2303.08533 [physics.acc-ph]].
- [21] F. Zimmermann, “LHC/FCC-Based Muon Colliders,” J. Phys. Conf. Ser. **1067** (2018) 022017.

- [22] M. W. Krasny, “The Gamma Factory proposal for CERN,” [arXiv:1511.07794 [hep-ex]].
- [23] F. Zimmermann, H. Aksakal, A. Aksoy, Z. Nergiz, “Free electron laser driven by a high-energy high-current energy-recovery linac,” in 10th International Particle Accelerator Conference, 2019.
- [24] J. Alwall, R. Frederix, S. Frixione, V. Hirschi, F. Maltoni, O. Mattelaer, H.-S. Shao, T. Stelzer, P. Torrielli, M. Zaro, “The automated computation of tree-level and next-to-leading order differential cross sections, and their matching to parton shower simulations,” J. High Energy Phys. **07** (2014) 079 [arXiv:1405.0301 [hep-ph]].
- [25] A. Buckley, J. Ferrando, S. Lloyd et al., “LHAPDF6: parton density access in the LHC precision era,” Eur. Phys. J. C **75** (2015) 132.
- [26] R. Brun, F. Rademakers, “ROOT — An object oriented data analysis framework,” Nucl. Instrum. Methods Phys. Res. A **389** (1997) 81.
- [27] H. Voss, A. Hoecker, J. Stelzer, F. Tegenfeldt, in “TMVA: Toolkit for Multivariate Data Analysis with ROOT,” XIth International Workshop on Advanced Computing and Analysis Techniques in Physics Research (ACAT) (2007), p. 40 [arXiv:physics/0703039].
- [28] Y. Coadou, “Boosted Decision Trees,” in P. Calafiura, D. Rousseau, K. Terao eds., “Artificial Intelligence in High Energy Physics,” World Scientific (2022) Singapore [arXiv:2206.09645 [physics.data-an]].
- [29] The CMS Collaboration, “Observation of a new boson at a mass of 125 GeV with the CMS experiment at the LHC,” Phys. Lett. B **716** (2012) 30 [arXiv:1207.7235 [hep-ex]].
- [30] The CMS Collaboration, “Observation of the diphoton decay of the Higgs boson and measurement of its properties,” Eur. Phys. J. C **74** (2014) 3076 [arXiv:1407.0558 [hep-ex]].
- [31] J. A. Aguilar-Saavedra, R. V. Herrero-Hahn, “Model-independent measurement of the top quark polarisation,” Phys. Lett. B **718** (2013) 983 [arXiv:1208.6006 [hep-ph]].
- [32] V. D. Barger, R. J. N. Phillips, “Collider Physics,” Addison-Wesley, Reading, Massachusetts, 1997.
- [33] Wolfram Research, Inc., “Mathematica,” Champaign, IL (2012).
- [34] M. Sas, J. Schoppink, “Event shapes and jets in  $e^+e^-$  and  $pp$  collisions,” Nucl. Phys. A **1011** (2021) 122195 [arXiv:2101.12367 [hep-ph]].

## A The effect of beam polarization

In the foregoing we always assumed unpolarized beams. However, future  $pe$  colliders are expected to have the capability to polarize lepton beams longitudinally, with polarizations reaching up to 80%. In this appendix we briefly discuss the effects of beam polarization on the asymmetry and its sensitivity to  $|V_{td}|$ .

For charged-current scattering, such as the signal processes (3), the cross-section dependence on longitudinal beam polarization is linear,

$$\sigma_{S\pm}^{\text{pol}} = (1 \pm \mathcal{P}_{e\pm})\sigma_{S\pm}, \quad (17)$$

with  $-1 \leq \mathcal{P}_{e\pm} \leq 1$  the beam polarization and  $\sigma_{S\pm}$  the cross section for the unpolarized process. Whereas in the unpolarized case the cross-section asymmetry (4) is also a charge asymmetry, in the polarized case we have to distinguish between the two. We define the cross-section asymmetry by analogy to (4) as,

$$A_{S,\sigma}^{\text{pol}} = \frac{\sigma_{S+}^{\text{pol}} - \sigma_{S-}^{\text{pol}}}{\sigma_{S+}^{\text{pol}} + \sigma_{S-}^{\text{pol}}}. \quad (18)$$

It will be convenient in what follows to define the quantities,

$$\overline{\mathcal{P}} = \frac{1}{2}(\mathcal{P}_{e+} + \mathcal{P}_{e-}), \quad \Delta\mathcal{P} = \frac{1}{2}(\mathcal{P}_{e+} - \mathcal{P}_{e-}). \quad (19)$$

We have  $-1 \leq \bar{\mathcal{P}}, \Delta\mathcal{P} \leq 1$ . Notice, however, that  $\bar{\mathcal{P}}$  and  $\Delta\mathcal{P}$  are not independent, since they must satisfy  $|\mathcal{P}_{e\pm}| = |\bar{\mathcal{P}} \pm \Delta\mathcal{P}| \leq 1$ . From the definitions (4), (17), (18), (19), we obtain the identity,

$$A_{S,\sigma}^{\text{pol}} = \frac{\bar{\mathcal{P}} + (1 + \Delta\mathcal{P})A}{1 + \Delta\mathcal{P} + \bar{\mathcal{P}}A}, \quad (20)$$

where  $A$  is the unpolarized asymmetry. Equation (20) shows that, as expected, beam polarization can induce a cross-section asymmetry even if  $A = 0$ . Such polarization asymmetry is independent of the interactions underlying the processes  $S^\pm$ . Equation (20) can be inverted, which motivates the following definition of charge asymmetry for polarized beams,

$$A_{S,\text{ch}}^{\text{pol}} = \frac{(1 + \Delta\mathcal{P})A_{S,\sigma}^{\text{pol}} - \bar{\mathcal{P}}}{1 + \Delta\mathcal{P} - \bar{\mathcal{P}}A_{S,\sigma}^{\text{pol}}}, \quad (21)$$

with  $A_{S,\sigma}^{\text{pol}}$  from (18). If  $\bar{\mathcal{P}} = 0$  we have  $\mathcal{P}_{e+} = -\mathcal{P}_{e-} \equiv \mathcal{P}$ ,  $\Delta\mathcal{P} = \mathcal{P}$ , and  $A_{S,\text{ch}}^{\text{pol}} = A_{S,\sigma}^{\text{pol}} = A$ , so that the charge asymmetry is independent of  $\mathcal{P}$ . In this case,  $\bar{\mathcal{P}} = 0$ , of which the unpolarized beams considered in the previous sections are a particular case, the effect of beam polarization on the sensitivity of the asymmetry to  $|V_{td}|$  can be readily quantified. Because the measurement uncertainty for the asymmetry is dominated by the statistical one, the cross-section dependence on  $\mathcal{P}$  will affect that sensitivity through the corresponding effect on the number of events. By using (17), we can write  $N^{\text{pol}} = \sigma_{S^\pm}^{\text{pol}} L_{\text{int}} = \sigma_{S^\pm} L_{\text{int}}^{\text{eff}}$ , with the “effective” integrated luminosity  $L_{\text{int}}^{\text{eff}} = (1 + \mathcal{P})L_{\text{int}}$ . Thus, for a run with  $L_{\text{int}} = 1/\text{ab}$ , in the limit case  $\mathcal{P} = +1$  we have  $L_{\text{int}}^{\text{eff}} = 2/\text{ab}$  and we can read the limits on  $|V_{td}|$  from table 2. For other values of  $L_{\text{int}}^{\text{eff}}$ , those limits can be obtained from table 2 by interpolation of the two luminosity values shown there.

## B Asymmetry in signal and background processes

Let  $S$  be the signal process, and  $B_k$ ,  $1 \leq k \leq N_B$ , background processes. We assume first that there is no interference among those processes, as is the case for reducible backgrounds with different number of  $b$  quarks in the final state. We then have,

$$\sigma_{S+B}^\pm = \sigma_S^\pm + \sum_{k=1}^{N_B} \sigma_{B_k}^\pm. \quad (22)$$

For a given process  $P$ , signal or background, we have the charge asymmetry (4), with (22) leading to the algebraic identity,

$$A_{S+B} = \tilde{A}_S + \sum_{k=1}^{N_B} \tilde{A}_{B_k}, \quad \tilde{A}_S = \rho A_S, \quad \tilde{A}_{B_k} = \rho \eta_k A_{B_k}, \quad (23)$$

$$\eta_k = \frac{\sigma_{B_k}^+ + \sigma_{B_k}^-}{\sigma_S^+ + \sigma_S^-}, \quad \rho = \frac{1}{1 + \sum_{k=1}^{N_B} \eta_k},$$

expressing the asymmetry of the total process  $S + B$  in terms of the asymmetries and cross sections of the individual processes  $S$  and  $B_k$ . We stress that the contributions to the total asymmetry  $A_{S+B}$  of the individual background asymmetries  $A_{B_k}$  are suppressed by the cross-section ratios  $\eta_k$ . If there is interference among the processes  $S$ ,  $B_k$ , the expression (23) holds in the approximation that such interference is small and can be neglected. The validity of (23) in those cases must be checked numerically.

## C Approximate normal distribution for the asymmetry

Let us consider the cross sections  $\sigma_\pm$  to be jointly normal distributed,

$$(\sigma_+, \sigma_-) \sim \mathcal{N} \exp \left( -\frac{1}{2(1-\rho^2)} \left( \frac{(\sigma_+ - \mu_{\sigma_+})^2}{\Delta_{\sigma_+}^2} - 2\rho \frac{(\sigma_+ - \mu_{\sigma_+})(\sigma_- - \mu_{\sigma_-})}{\Delta_{\sigma_+} \Delta_{\sigma_-}} + \frac{(\sigma_- - \mu_{\sigma_-})^2}{\Delta_{\sigma_-}^2} \right) \right) \quad (24)$$

where  $\mu_{\sigma_\pm}$  are the means and  $\Delta_{\sigma_\pm} > 0$  the standard deviations for  $\sigma_\pm$ , and  $-1 < \rho < 1$  the correlation parameter. We assume that the probability for  $\sigma_\pm$  to be negative is exponentially small, which means that

$0 < \Delta_{\sigma_{\pm}} \ll \mu_{\sigma_{\pm}}$ . We assume also that the mean asymmetry is small:  $|(\mu_{\sigma_+} - \mu_{\sigma_-})/(\mu_{\sigma_+} + \mu_{\sigma_-})| \lesssim 0.02$ . Then, to a very good approximation, the asymmetry  $A = (\sigma_+ - \sigma_-)/(\sigma_+ + \sigma_-)$  is normally distributed with

$$\mu_A = \frac{\mu_{\sigma_+} - \mu_{\sigma_-}}{\mu_{\sigma_+} + \mu_{\sigma_-}} , \quad \Delta_A^2 = \frac{\Delta_{\sigma_+}^2 + \Delta_{\sigma_-}^2 - 2\rho\Delta_{\sigma_+}\Delta_{\sigma_-}}{(\mu_{\sigma_+} + \mu_{\sigma_-})^2} . \quad (25)$$

In the particular case of the statistical fluctuations of a Poisson process we have  $\Delta_{\sigma_{\pm}}/\mu_{\sigma_{\pm}} = 1/\sqrt{N_{\pm}}$ , where  $N_{\pm} = \sigma_{\pm}L_{\text{int}}$  is the number of events, assuming for simplicity the same integrated luminosity  $L_{\text{int}}$  for  $pe^+$  and  $pe^-$  collisions. We then have from (25),

$$(\Delta_A^2)_{\text{stat}} = \frac{1}{(N_+ + N_-)^2} \left( N_+ + N_- - 2\rho\sqrt{N_+N_-} \right) \simeq \frac{1 - \rho}{N_+ + N_-} , \quad (26)$$

where in the last step we used the approximate equality  $N_+ \simeq N_-$  due to the smallness of the asymmetry. Equation (26) gives the statistical uncertainty for  $A$ .